IEEE Access
Multidisciplinary ⋮ Rapid Review ⋮ Open Access Journal

Received January 4, 2020, accepted January 20, 2020, date of publication January 28, 2020, date of current version February 6, 2020.

Digital Object Identifier 10.1109/ACCESS.2020.2970026

A Convolutional Neural Network for Prediction of Laser Power Using Melt-Pool Images in Laser Powder Bed Fusion

OHYUNG KWON[1], HYUNG GIUN KIM[1], WONRAE KIM[1], GUN-HEE KIM[1], AND KANGIL KIM[2], (Member, IEEE)

[1]Additive Manufacturing R&D Group, Gangwon Regional Division, Korea Institute of Industrial Technology, Gangneung 25440, South Korea
[2]School of Electrical Engineering and Computer Science, Gwangju Institute of Science and Technology, Gwangju 61005, South Korea

Corresponding author: Kangil Kim (kangil.kim.01@gmail.com)

This work was supported by the National Research Foundation of Korea (NRF) grant funded by the Korean Government(MSIT) under Grant 2019R1A2C1091077.

ABSTRACT In laser powder bed fusion, a convolutional neural network could build a good regression model to predict a laser power value from a melt-pool image. To empirically validate it, we used the acquired image data from a monitoring system inside metal additive manufacturing equipment and optimally configured a convolutional network by the grid search of hyper-parameters. The proposed network showed only 0.12 % of test images were out of the criterion for judging the predicted laser power value to be reliable and showed more accurate results than deep feed-forward neural network in the prediction of laser power states unseen in training steps. We expect that the proposed model could be utilized to discover the problematic position in additive-manufactured layers causing defects during a process.

INDEX TERMS Convolutional neural network, metal additive manufacturing, laser powder bed fusion, melt-pool image, process monitoring.

I. INTRODUCTION

Metal additive manufacturing (AM) is a suitable technology to produce specific parts which are difficult to be formed by a traditional fabrication method such as casting or cutting because of much more freedom of design. Metal AM offers advantages to design the complex geometry and to reduce the weight and the number of parts. It is the reason why aerospace and energy industries have adopted metal AM to produce parts of their aircraft engine and gas turbine. Laser powder bed fusion is a metal AM technique to proceed following two steps repeatedly on every layer. First, metal powders of several ten-micrometer diameter are spread on a metallic plate. Second, selectively focusing a laser beam spot on the cross-section layer of a part melts powders, and the molten region rapidly cool down. Unexpected phenomena of powder distribution and melt-pool dynamics in AM process cause defects in the part such as porosity, cracking and layer delamination which act to worsen the part reliability and are confirmed by only the destruction of part. The instant that these quality problems occur could be identified by in-situ and real-time monitoring of a melt-pool.

The melt-pool is a locally melting zone generated by short-time laser irradiation on powder particles. The melt-pool has been utilized to monitor AM process by several researchers [1]–[5]. The visible light is emitted from the melt-pool, and high-speed camera could capture the only coaxial light with a laser path. Because the light intensity and the shape of melt-pool are determined by process parameters and circumstance, utilizing images of melt-pools could be considered whether the process status is normal or abnormal without the interruption to AM process and the destruction of part. However, when an AM part is completely built by several ten thousand of layers and over, several hundreds of gigabyte files of melt-pool images and more are saved. It is impossible to perfectly judge normal or abnormal melt-pool images by human thinking or arithmetic algorithm because the images show various shapes of melt-pools despite the same process condition, but a deep neural network could be an appropriate solution to correctly judge the state of melt-pool one-by-one.

A deep neural network (DNN) is a machine learning method to stack multiple hidden layers of linear combinations of inputs with nonlinear activation functions.

The associate editor coordinating the review of this manuscript and approving it for publication was Ming Luo.

This data-driven model approach has shown good performance in modelling with huge amount of data and enough computing power without expert knowledge about features and model structures in manufacturing applications including material science [6]–[10]. In the case of DNN for image classification, when the intensity data of pixels pass many hidden layers of DNN consecutively, the extracted low-level features such as lines and edges of a raw image change to high-level features such as shapes combined by lines and finally, DNN provides the probability to infer a certain object from these feature information [11].

Machine learning technology including DNNs has been recently applied to AM process monitoring fields. Song et al. [12] used various machine learning algorithms to predict the metal compositions using laser-induced plasma spectroscopy. Scime and Beuth [13] used a convolutional neural network for detection and classification of powder spreading anomalies. Scime and Beuth [14] also used machine learning to detect keyholing porosity and balling instabilities using melt pool images. Shevchik et al. [15] used a convolutional neural network for in situ quality monitoring using acoustic emission recorded during AM process. Similar to former researches, prior study by the authors [16] used a feed-forward neural network (FFNN) to create a regression model which predicted a certain laser power value from a melt-pool image gathered by a high-speed camera in 6 laser power conditions between 100, 150, 200, 250, 300 and 350 W. The FFNN provided inference success rate over 99% in classification approach but showed poor prediction of laser power values in regression approach, especially in leave-one-out test completely excluding data categorized as a class from training data and then predicting it in test. Because acquiring melt-pool images of all laser power conditions is restricted by resource limitation, the poor prediction for the un-acquired and unlabeled image set could be reluctant to apply DNN for real industrial fields.

A CNN is a popular DNN in the application of image classification. Differently to FFNN, a CNN apply more small networks, called as filter, to smaller regions on an input image to extract localized features and therefore we can control the generalization level of extracted features at each layer [11], [17].

The focused feature extraction on a small region is suitable to laser power prediction from the melt-pool images because the image of a melting spot is usually observed in a very small area and their difference are mostly concentrated on the edges of a circle. The strong locality of features to distinguish cases is expected to point better in CNN than FFNN. This dependency of close visual features can be represented in CNN more naturally compared to FFNN assuming all possible dependencies, and therefore finely tuned CNN may have the model regularized close to the real model.

In this study, the high-speed camera inside a metal AM equipment captured 199,473 melt-pool images from coaxial visible light during AM process as laser power condition was changed. Various regression models using CNNs were trained and tested to predict the laser power values from the gathered melt-pool images. Root mean squared error and the coefficient of the determination (R^2) of CNNs were analyzed to find the best-performed model. The results of inference failure rate and leave-one-out evaluation for an FFNN and CNNs were also compared.

II. METHODS

A. MELT-POOL IMAGE DATA ACQUISITION

The melt-pool images for the prediction of laser power values were collected by the melt-pool monitoring system of metal additive manufacturing equipment which was developed by WINFORSYS. The optical elements of the monitoring system were a dichroic mirror, a galvanometer scanner, an F-theta lens and a high-speed camera. The laser beam of 1075 nm wavelength and 100 μm beam size was reflected by the dichroic mirror and the galvanometer scanner, and finally irradiated on stainless steel (SUS316L) powders having D_{50} of 28.5 μm. The laser beam fused the powders and formed a melt-pool which emitted visible light. The only co-axially aligned visible light (450∼900nm wavelength) at the galvanometer mirror position was transmitted through the optical elements and arrived at the high-speed camera. When the laser beam was scanned along the programmed path, the system saved the images of 512 × 512 pixels and 8bit gray scale using the high-speed camera of 2.5 kHz framerates. The monitoring system simultaneously acquired not only a melt-pool image but also a position data of x- and y-coordinate, so we could know the location information where a melt-pool image was captured. Laser power was the only process variable to change the melt-pool shapes when cuboid specimens of 8.5 mm in depth and 8.5 mm in width and 4 mm in height were fabricated on the SUS316L-based build plate. The melt-pool images were saved during AM process between the 50th layer and the 99th layer of total 150 layers. The rest of process variables were fixed. Hatching distance was 100 μm. Scan speed was 2.5 m/s. Layer thickness was 30 μm. Process gas was argon atmosphere with oxygen density under 0.1%. Hatching strategy was the rotation of a stripe pattern through 67 degrees for each layer. Fig. 1 shows the schematic diagram for melt-pool monitoring, and Fig. 2 shows the produced specimens and melt-pool images for each laser power condition. All melt-pool images and the details of the experiment settings used in this study were the same as those used in the reference [16].

Six laser powers which were 100, 150, 200, 250, 300 and 350 W were utilized to gather various melt-pool images. The images were clipped into 60 × 60 pixels to remove useless black areas. Summing up 3,600 pixels' intensities of each image and calculating the histogram of those values were used to filter garbage images having blurred and shattered shapes. Table 1 shows the ratios of images which occupied intervals of histograms for 'the sum of pixel intensity' to total images. About 70% of total images were distributed among a narrow interval regardless of the laser power conditions, and

TABLE 1. The ratio of images which occupied the intervals of 'sum of pixel intensity' histogram to the number of total images metal additive manufacturing equipment.

Laser power (W)	Interval of 'sum of pixel intensity' histogram ($\times 10^4$)			The number of total images
	Ratio of images which occupied the interval (%)			
100	**20.8 ~ 22.8**	**22.8 ~ 23.4**	**23.4 ~ 24.6**	33,793
	25.2	72.3	2.5	
150	**20.8 ~ 24.0**	**24.0 ~ 24.6**	**24.6 ~27.2**	33,087
	27.5	66.9	5.6	
200	**20.5 ~ 24.5**	**24.5 ~ 26.0**	**26.0 ~ 28.0**	33,193
	23.2	75.4	1.4	
250	**20.5 ~ 25.5**	**25.5 ~ 27.0**	**27.0 ~ 31.5**	33,091
	24.7	70.1	5.2	
300	**20.5 ~ 26.5**	**26.5 ~ 28.5**	**28.5 ~ 33.0**	33,194
	25.3	69.7	5.0	
350	**20.0 ~ 27.0**	**27.0 ~ 31.0**	**31.0 ~ 37.0**	33,115
	21.5	74.2	4.3	

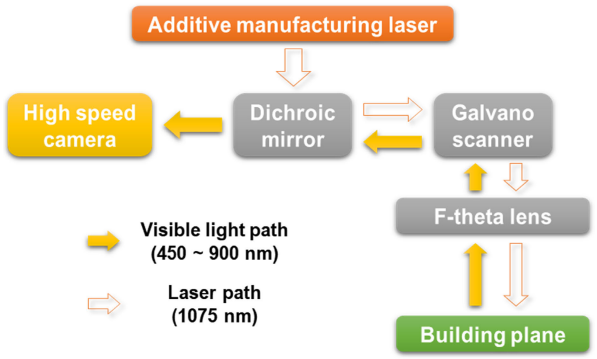

FIGURE 1. Schematic diagram of melt-pool monitoring system inside.

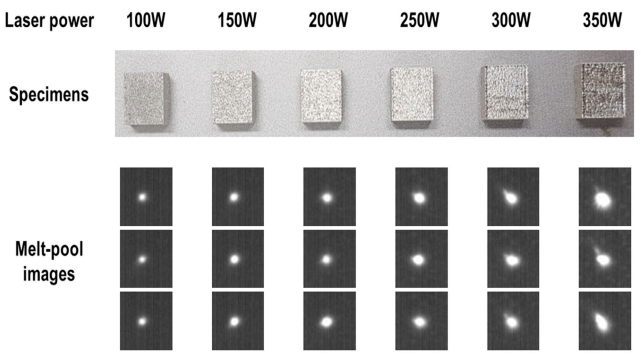

FIGURE 2. Produced specimens and melt-pool images for each laser power condition.

those images were used for deep learning as normal images in this study. For each laser power condition, 22,000 images among whole images were randomly selected. 17,600 of 22,000 images for 'training' were used to train the model, 2,200 of 22,000 images for 'validation' to detect the overfitting status of a training model and 2,200 of 22,000 images for 'test' to test the model. One melt-pool image was labeled one laser power value. Therefore, total 132,000 labeled images were used for training, validating, testing deep neural networks.

B. STRUCTURES AND EVALUATION OF DEEP NEURAL NETWORK

A CNN worked as the core component to predict the laser power value based on the melt-pool image of 60 × 60 pixels. We considered three cases of the input size of filters and three cases of the channel sizes of convolutional (Conv) layers respectively, so total nine network structures were tested to find out the best network. The different network structures were summarized in Table 2 and Table 3. The three cases of filters for Conv layers were 3×3, 5×5 and 7×7. A filter size was fixed in every layer of each structure except the last layer. The number of Conv layers was fixed at 4. For all Conv layers, stride was set on 1 and there was no zero-padding. Max pooling layers were positioned after only first three Conv layers from the input side. For all max pooling layers, stride was set on 2 and zero-padding was applied. The output size of the last Conv layer was adjusted to 1×1 by changing the input size of the last filter. The channel size n of l^{th} Conv layer from the input side was as follows:

$$n = (l+1)^k \tag{1}$$

l is the layer number of a Conv layer from the input side. Three cases of k were considered ($k = 2, 3, 4$). The node size of a fully connected (FC) layer was the previous layer's node size divided by 5, and it was repeated until the node size became 25. When k was 2, there was only one FC layer. The node size of the last FC layer was 1 for all cases

TABLE 2. Feature map size varied by the filter size condition of convolutional layers.

Filter size	Layer 1 (Conv→ Maxpool)	Layer 2 (Conv→ Maxpool)	Layer 3 (Conv→ Maxpool)	Layer 4 (Conv)
3×3	58×58 → 29×29	27×27 → 14×14	12×12 → 6×6	1×1 (Filter 6×6)
5×5	56×56 → 28×28	24×24 → 12×12	8×8 → 4×4	1×1 (Filter 4×4)
7×7	54×54 → 27×27	21×21 → 11×11	5×5 → 3×3	1×1 (Filter 3×3)

TABLE 3. Channel size of each convolutional (Conv) layer and node size of each fully connected (FC) layer. The channel size n of Conv layers is varied by k value of the equation (1).

k	Layer 1 (Conv)	Layer 2 (Conv)	Layer 3 (Conv)	Layer 4 (Conv)	Layer 5 (FC)	Layer 6 (FC)	Layer 7 (FC)
2	4	9	16	25	1		
3	8	27	64	125	25	1	
4	16	81	256	625	125	25	1

of k. The number of total layers increased one by one as k value increased. At each layer, after the output of a previous layer were weighted and biased, batch normalization method was applied for regularization and reducing learning time. Its algorithm was to normalize the output using the mean and the variance of one batch and introduce new weight and bias to be learned for the normalized output [17]. To transform the normalized output of a previous layer to a nonlinear data, ReLU (Rectified Linear Unit) was used as an activation function at each layer. ReLU is identity for all positive values and zero for all negative values and is effective at avoiding the vanishing gradient problem [18]. Afterwards the extracted features were subsampled through a max pooling layer.

Fig. 3 shows the flowchart training a CNN. The network f of total m hidden layers was composed of m weight matrices $W = \{W_1, \cdots, W_m\}$ and m bias vectors $b = \{b_1, \cdots, b_m\}$. At first, all weight matrices were initialized by He's initialization method which was a proper initialization method because it could avoid to reducing or magnifying the magnitude of input data exponentially when an activation function was ReLU [19]. Bias vectors were initialized to zero. Total training images, i.e. 6 laser powers × 17,600 training images = 105,600 images, were subdivided to a batch to learn the network f because of computing power. After the network f randomly estimated an output h_i for an image x_i, h_i was compared to label y_i using a cost function. The cost, root mean squared error (RMSE) plus L2 regularization term was calculated as follows:

$$\text{cost} = \sqrt{\sum_{i=1}^{N} \frac{(y_i - h_i)^2}{N}} + \lambda \cdot \sum_{i=1}^{m} |W_i|^2 \qquad (2)$$

h_i is the predicted output for i^{th} image. y_i is the label for i^{th} image. N is the number of images for one batch, which was 1,100 for training, 2,200 for validation and test. L2 regularization $\lambda \cdot \sum_{i=1}^{m} |W_i|^2$ with weight value (λ) of 0.0001 was added to RMSE for preventing the overfitting [20]. To train the network f, we used AdaDelta optimizer which is a gradient-based optimizer using second derivative known as momentum [21]. After the gradient and the momentum of the network f were evaluated, this optimizer updated network parameters using dynamic programming to store partial evaluation results which is identical to backpropagation. Early stopping algorithm was employed for the validation image set to avoid overfitting and save the best network parameter values [20], was called every 10^{th} epoch and updated the minimum of the cost for validation set as the epoch proceeded. When the minimum of the cost for validation set was maintain during 5,000 epochs, it is saved as the best parameter values of the network f that the parameter values of the epoch at which the minimum of the cost for validation appeared.

The different neural networks evaluated their regression performances using test images and ten-fold cross-validation. The average and standard deviation of RMSE and R^2 in ten-fold cross-validation were used to find the best model of CNN structures which could extremely reduce errors between the predicted value and the label. The coefficient of determination R^2 gave the information about the goodness of fit for the network structures. R^2 was calculated as follows:

$$R^2 = 1 - \left(\frac{\sum_{i=1}^{N} (y_i - h_i)^2}{\sum_{i=1}^{N} (y_i - \bar{y})^2} \right) \qquad (3)$$

$\bar{y}$ is the mean of all labels. N is 13,200 calculated by multiplying 2,200 test images and 6 laser power conditions. If RMSE is closed to 0 and R^2 is closed to 1, it means that the predicted value for images perfectly fits the laser power value. In previous study, the optimization of FFNN was conducted for same melt-pool image sets used for this study and the best structure of FFNN was derived [16]. Fig. 4 shows the best-performed FFNN (FFNN-10LK2) to predict the laser power from a melt-pool image. It was comprised of 10 hidden layers of which the number of nodes n was dropped by equation (4) as follows:

$$n = 3600 \cdot m^2 \qquad (4)$$

m decreases from 0.9 to 0.1 with the increase of the layer number from 1 to 9. '3600' means total pixels of an image. The layer number 0 was input layer and the layer number 10 was output layer. The inference performances of CNNs and the FFNN were evaluated by the inference failure rate which was a ratio of the number of images to be out of the correct inference range to 2,200 test images for each laser

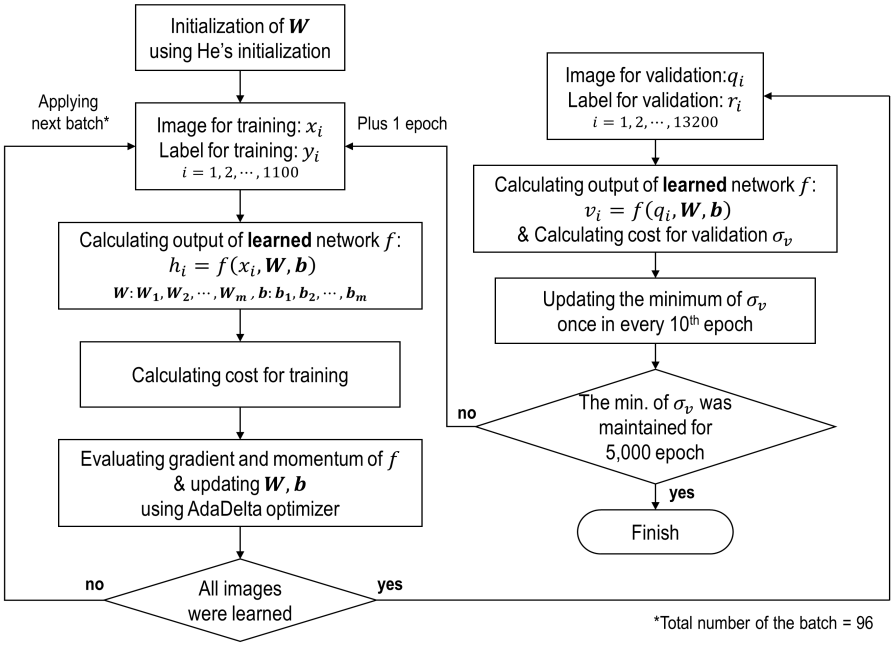

FIGURE 3. Flowchart to train a CNN for predicting a laser power from an image.

power using ten-fold cross-validation. The correct inference range was defined as follows:

$$\varepsilon = \frac{|h_{i,t} - y_{i,t}|}{y_{i,t}} \times 100 < \varepsilon_{th} \tag{5}$$

$y_{i,t}$ corresponds to the label of a test image, $h_{i,t}$ corresponds to the predicted laser power value using the finally learned neural network and ε_{th} corresponds to the threshold value for inference successes decision. When the error ε was over ε_{th}, it was decided the inference failure. The threshold value ε_{th} of the criterion for decision were chosen by 3 and it came from maximum long-term power instability of laser power generator datasheet (YLR-AC 400W) because this tolerance is commonly accepted by the equipment producer and it is the criterion for judging the laser power value to be reliable.

Leave-one- out (LOO) method was also used to evaluate the inference performance. The procedure of LOO method was to train a certain deep neural network with training images of only 5 laser power conditions except 1 condition and after that, to test the neural network with test images of all 6 laser power conditions including the omitted condition. This method was effective to evaluate the performance that how well a deep neural network could estimate an unknown state between already known states. Therefore, LOO method was only evaluated between 150 W and 300 W because there were no lower and upper limit of 100 W and 350 W condition. The optimization results of CNNs and inference performance results of deep neural networks were described in Section III.

III. RESULTS AND DISCUSSION

Varying the filter size and the channel size of Conv layers, the results of RMSE and R^2 were derived in Table 4. When the filter size was 3×3, increasing the channel size decreased RMSE. However, for 5×5 or 7×7 filter size, the lowest RMSE was derived when k was 3. All R^2 of nine CNNs were highly close to 1, but R^2 for 3×3 filter size was further to 1 than other filter sizes. The case that the filter size and the channel size were over the values of Table 4 spent much time on training the model. For the variation of the filter size and the channel size, RMSE was sensitive, but R^2 was robust. Therefore, the CNN of 7×7 filter size and k value of 3 (CNN-F7K3) with the lowest RMSE was chosen as the best performed structures in this study. Table 5 shows the inference failure rate of FFNN-10LK2 and CNN-F7K3. The averaged inference failure rates were 0.283 % for FFNN-10LK2 and 0.778 % for CNN-F7K3.

Although the CNN performed well with the averaged inference success rates of over 99 %, the FFNN showed higher accuracy. It is generally known that a CNN have good ability to extract detailed features of complicated images, but in this study, the increase of inference failure rate meant that CNN-F7K3 sensitively reacted to the shape variation of melt-pool images and erroneously predicted the laser power values of melt-pool images.

A sigmoid form function which returns the value monotonically increasing from 0 to 1 for the input of all real numbers was introduced to reduce the sensitivity of CNN-F7K3. As the output value of CNN-F7K3 entered a sigmoid form function once more, the fluctuation of the final predicted value could be reduced because large errors were suppressed. The sigmoid form function which had two updating variables was applied as follows:

$$h_i = \frac{a}{1 + exp\,(b \cdot z_i)} \tag{6}$$

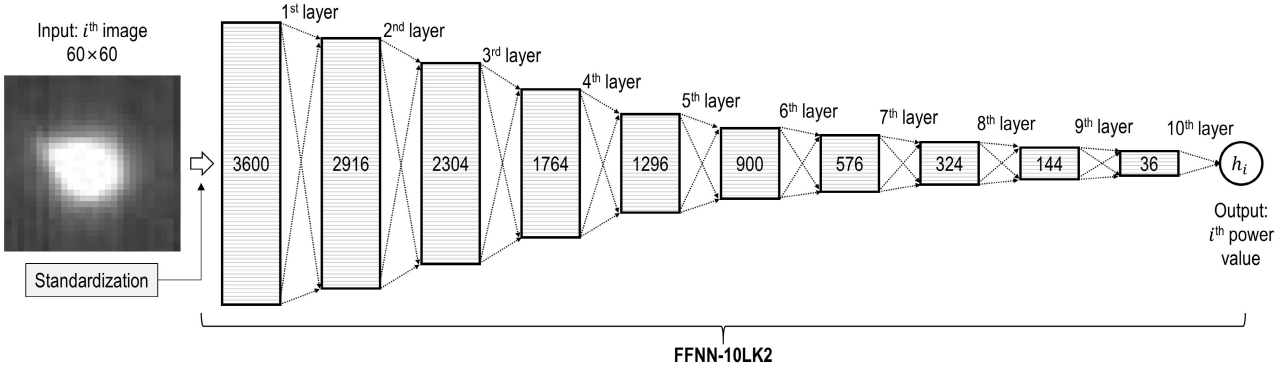

FIGURE 4. Best-performing FFNN (FFNN-10LK2) derived in preliminary results of our work [16].

TABLE 4. Average (μ) and standard deviation (σ) of RMSE and R^2 varied by the filter size and the k value of the equation (1).

Filter size (F)	k (K)	RMSE		R^2	
		μ	σ	μ	σ
3×3	2	3.471	1.692	0.9984	0.00078
	3	2.419	1.630	0.9990	0.00081
	4	1.835	1.287	0.9932	0.01748
5×5	2	2.025	0.6081	0.9986	0.00081
	3	1.913	0.8091	0.9993	0.00036
	4	1.940	0.9945	0.9992	0.00028
7×7	2	1.932	1.0513	0.9984	0.00162
	3	1.758	0.6284	0.9994	0.00030
	4	1.966	1.2149	0.9993	0.00035

a and b were updated at the same time when weights and biases of the CNN were updated. z_i is the output value of CNN-F7K3 for i^{th} image. h_i is the finally predicted output of CNN-F7K3-Sig for i^{th} image. Fig. 5 shows the CNN of 7×7 filter size and k value of 3, of which the last layer was connected to the sigmoid form function (CNN-F7K3-Sig). The results of RMSE and R^2 of CNN-F7K3-Sig were derived in Table 6 and the results comparing CNN-F7K3 and CNN-F7K3-Sig were shown in Fig. 6. Compared to CNN-F7K3, CNN-F7K3-Sig decreased the average of RMSE by 50% and increased the average of R^2 by 0.03%.

Applying the sigmoid form function was effective to reduce the fluctuation of the predicted value as mentioned above.

Table 7 shows the inference failure rate of CNN-F7K3-Sig and Fig. 7 shows the inference failure rates of FFNN-10LK2, CNN-F7K3 and CNN-F7K3-Sig for each laser power value. The average of inference failure rate of CNN-F7K3-Sig was 0.123 %, and especially the inference failure rate for 100 W drastically decreased from 3.16 % to 0.33 %. The inference

TABLE 5. Inference failure rate of the proposed deep neural networks for each laser power condition.

Model	100 W	150 W	200 W	250 W	300 W	350 W
FFNN-10LK2	1.10 %	0.41 %	0.01 %	0.10 %	0.02 %	0.09 %
CNN-F7K3	3.16 %	0.29 %	0.20 %	0.29 %	0.40 %	0.33 %

TABLE 6. Average (μ) and standard deviation (σ) of RMSE and R^2 of the convolutional neural network of which the last layer was connected to the sigmoid function.

Model	RMSE		R^2	
	μ	σ	μ	σ
CNN-F7K3-Sig	0.871	0.4865	0.9997	0.00017

TABLE 7. Inference failure rate of the convolutional neural network of which the last layer was connected to the sigmoid function.

Model	100 W	150 W	200 W	250 W	300 W	350 W
CNN-F7K3-Sig	0.33 %	0.09 %	0.18 %	0.07 %	0.07 %	0.00 %

performance of CNN-F7K3-Sig was also improved for all laser powers comparing with CNN-F7K3 and was better than FFNN-10LK2 for most laser powers.

The FFNN-10LK2 could correctly inferred 99 % and over of test images, but the model was not good at the LOO evaluation. Fig. 8 shows the averages of predicted laser power for each omitted image set (only 150 W, 200 W, 250 W and 300 W) of FFNN-10LK2 and CNN-F7K3-Sig. Because there was no either the lower label than 100 W or the upper label than 350 W, it is impossible to correctly predict these laser power values from images of 150∼300 W. The dash line of

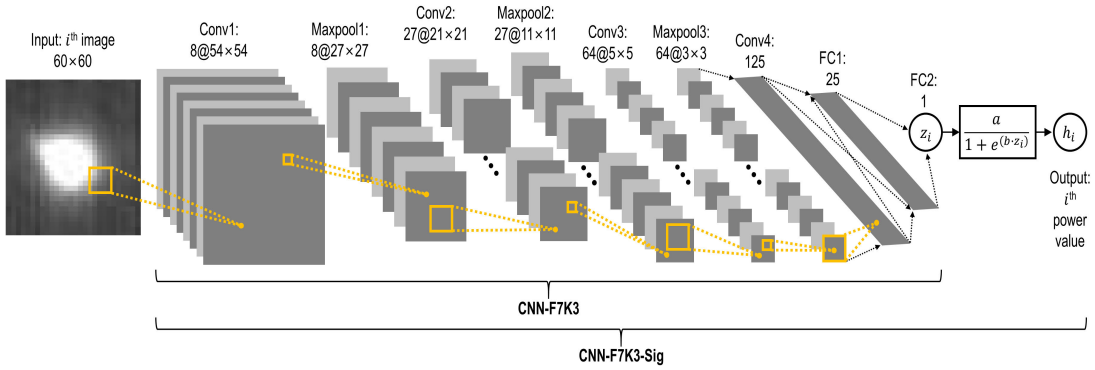

FIGURE 5. CNN of 7×7 filter size and k value of 3, of which the last layer was connected to the sigmoid form function.

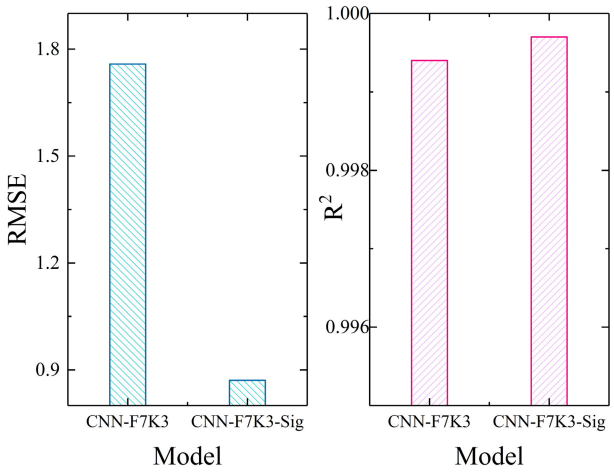

FIGURE 6. Averaged RMSE and R^2 of CNN-F7K3 and CNN-F7K3-Sig.

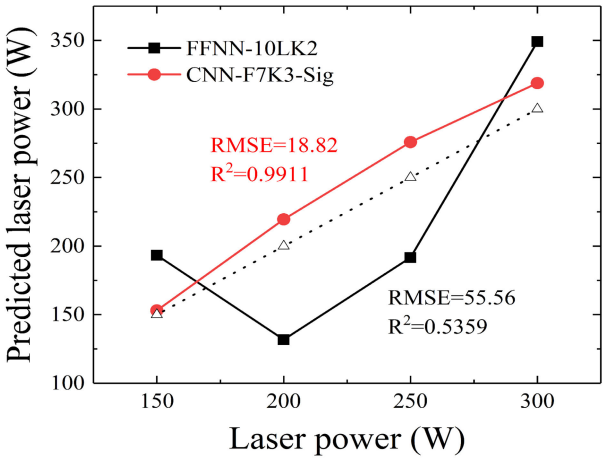

FIGURE 8. LOO evaluation results for each omitted image set (150 W, 200 W, 250 W and 300 W) of FFNN-10LK2 and CNN-F7K3-Sig.

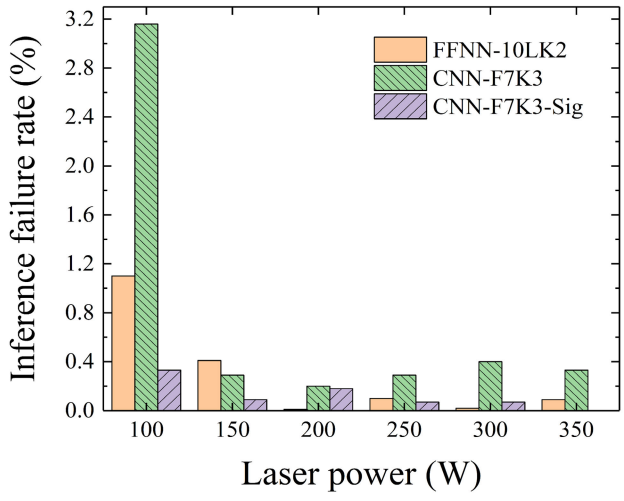

FIGURE 7. Inference failure rate of FFNN-10LK2, CNN-F7K3 and CNN-F7K3-Sig for data categorized by each laser power condition.

Fig. 8 meant the perfectly predicted laser power values for the omitted labels. The predicted values of CNN-F7K3-Sig model were closer to the dash line than FFNN-10LK2 and were distributed on a straight line. RMSE and R^2 of LOO evaluations for FFNN-10LK2 were 55.56 and 0.54. However, the CNN achieved the high performance of LOO evaluation. RMSE and R^2 of LOO evaluations for CNN-F7K3-Sig was 18.82 and 0.99. If the model provides that RMSE is smaller and R^2 of the LOO evaluation is close to 1, it meant the model could predict the laser power value for the unseen image sets more precisely.

The FFNN could correctly infer the melt-pool images of only already learned labels but had poor performance to hardly infer the melt-pool images which were not in the label sets for deep learning. However, the CNN showed good inference performance whether the melt-pool images were in the label sets or not. The regularization effect by the filter of CNN derived better performance for LOO evaluation. Because it is impossible to gather melt-pool images of all laser power conditions, the correct prediction for the unlabeled image set of unseen state is required to utilize the model in industrial sites. Therefore, the CNN is appropriate for monitoring the melt-pool images one by one rather than the FFNN.

Additionally, the computational efficiencies of networks were compared as shown in Table 8, which were measured based on average running time at which training networks took to complete. For example, the model name of 'CNN of 3×3 filter size and k value of 2' was abbreviated to

TABLE 8. Averaged running time at which training the network took to complete.

Model	Time (min.)	Model	Time (min.)
CNN-F3K2	3,368	**CNN-F7K2**	1,417
CNN-F3K3	2,505	**CNN-F7K3**	2,064
CNN-F3K4	2,882	**CNN-F7K4**	2,783
CNN-F5K2	2,026	**CNN-F7K3-Sig**	1,982
CNN-F5K3	2,031	**FFNN-10LK2**	1,175
CNN-F5K4	2,966	-	-

'CNN-F3K2'. The NVIDIA TITAN Xp GPU was used for training a network. Increasing a filter map size usually took short running time and increasing a channel size took long running time roughly. The running time of CNN-F7K3-Sig was like CNN-F7K3 even if the last layer was connected to the sigmoid form function. The running time of FFNN-10LK2, however, was shorter than any other network.

The proposed network will be used to judge the defects of parts, the reliability of AM process, and the accuracy of laser power. The type of most defects occurred during AM process is a pore which is formed by the lack or the excess of an energy required to melt powders properly. A melt-pool image is also changed by the amount of the energy transferred into powders. Using the CNN can distinguish the energy value precisely from a melt-pool image and thus infer that a defect occurs at the position where the predicted laser power is suddenly and excessively changed. This method is also used to confirm the reliability of AM process including powder coating and laser irradiation because all melt-pool images can be easily compared by the laser power values predicted in real time and it can even define a standard trend using images. Abnormal laser output can be also detected by the CNN because an abrupt change of laser output significantly affects a melt-pool if other variables like powders, a chamber atmosphere, a plate temperature, etc. maintain normal conditions. The proposed network will also be applied to a feedback control system for AM process. When the predicted laser power value at a certain position is out of the correct inference range, powder coating and laser irradiation could be re-proceeded at the problematic position and AM product could be repaired during the process. Still there are problems to be solved for applying the CNN to real AM field, which are how more high-quality melt-pool images are acquired and how useful or useless images are distinguished in a preprocessing step.

IV. CONCLUSION

The regression model to predict a laser power value from a melt-pool image was studied through adapting CNNs to this problem. Total 132,000 melt-pool images gathered by high speed camera varying laser power for AM process were used to train, validate and test models. Although the best-performing network structure was proposed through parametric experiments of nine CNNs, the FFNN still showed higher inference accuracy because the CNN sensitively reacted to the variation of melt-pool images and erroneously predicted the laser power values of melt-pool images. A sigmoid form function was applied to the last layer of the CNN to reduce the sensitivity. Using a sigmoid form function decreased the inference failure rate for all laser powers, and especially, it for the images of 100 W drastically decreased. The proposed CNN (CNN-F7K3-Sig) also provided higher inference success rate on the LOO evaluation even if the melt-pool images were not in the label sets for deep learning. Therefore, it is expected that the prediction of laser power values from melt-pool images using the proposed model could be used to find the problematic position without destructive tests of AM product.

REFERENCES

[1] S. Berumen, F. Bechmann, S. Lindner, J.-P. Kruth, and T. Craeghs, "Quality control of laser- and powder bed-based Additive Manufacturing (AM) technologies," *Phys. Procedia*, vol. 5, pp. 617–622, Aug. 2010.

[2] T. Craeghs, S. Clijsters, J.-P. Kruth, F. Bechmann, and M.-C. Ebert, "Detection of process failures in layerwise laser melting with optical process monitoring," *Phys. Procedia*, vol. 39, pp. 753–759, Nov. 2012.

[3] B. Lane, S. Moylan, E. P. Whitenton, and L. Ma, "Thermographic measurements of the commercial laser powder bed fusion process at NIST," *Rapid Prototyping J.*, vol. 22, no. 5, pp. 778–787, Aug. 2016.

[4] F. Wirth, S. Arpagaus, and K. Wegener, "Analysis of melt pool dynamics in laser cladding and direct metal deposition by automated high-speed camera image evaluation," *Additive Manuf.*, vol. 21, pp. 369–382, May 2018.

[5] S. Coeck, M. Bisht, J. Plas, and F. Verbist, "Prediction of lack of fusion porosity in selective laser melting based on melt pool monitoring data," *Additive Manuf.*, vol. 25, pp. 347–356, Jan. 2019.

[6] R. Liu, A. Kumar, Z. Chen, A. Agrawal, V. Sundararaghavan, and A. Choudhary, "A predictive machine learning approach for microstructure optimization and materials design," *Sci. Rep.*, vol. 5, no. 11441, pp. 1–12, Jun. 2015.

[7] B. L. Decost, H. Jain, A. D. Rollett, and E. A. Holm, "Computer vision and machine learning for autonomous characterization of am powder feedstocks," *J. Mach.*, vol. 69, no. 3, pp. 456–465, Mar. 2017.

[8] M. Ferguson, R. Ak, Y.-T.-T. Lee, and K. H. Law, "Automatic localization of casting defects with convolutional neural networks," in *Proc. IEEE Int. Conf. Big Data*, Boston, MA, USA, Dec. 2017, pp. 1726–1735.

[9] D.-H. Kim, T. J. Y. Kim, X. Wang, M. Kim, Y.-J. Quan, J. W. Oh, S.-H. Min, H. Kim, B. Bhandari, I. Yang, and S.-H. Ahn, "Smart machining process using machine learning: A review and perspective on machining industry," *Int. J. Precis. Eng. Manuf.-Green Tech.*, vol. 5, no. 4, pp. 555–568, Aug. 2018.

[10] M. Mozaffar, A. Paul, R. Al-Bahrani, S. Wolff, A. Choudhary, A. Agrawal, K. Ehmann, and J. Cao, "Data-driven prediction of the high-dimensional thermal history in directed energy deposition processes via recurrent neural networks," *Manuf. Lett.*, vol. 18, pp. 35–39, Oct. 2018.

[11] V. Sze, Y.-H. Chen, T.-J. Yang, and J. S. Emer, "Efficient processing of deep neural networks: A tutorial and survey," *Proc. IEEE*, vol. 105, no. 12, pp. 2295–2329, Dec. 2017.

[12] L. Song, W. Huang, X. Han, and J. Mazumder, "Real-time composition monitoring using support vector regression of laser-induced plasma for laser additive manufacturing," *IEEE Trans. Ind. Electron.*, vol. 64, no. 1, pp. 633–642, Jan. 2017.

[13] L. Scime and J. Beuth, "A multi-scale convolutional neural network for autonomous anomaly detection and classification in a laser powder bed fusion additive manufacturing process," *Additive Manuf.*, vol. 24, pp. 273–286, Dec. 2018.

[14] L. Scime and J. Beuth, "Using machine learning to identify *in-situ* melt pool signatures indicative of flaw formation in a laser powder bed fusion additive manufacturing process," *Additive Manuf.*, vol. 25, pp. 151–165, Jan. 2019.
[15] S. Shevchik, C. Kenel, C. Leinenbach, and K. Wasmer, "Acoustic emission for *in situ* quality monitoring in additive manufacturing using spectral convolutional neural networks," *Additive Manuf.*, vol. 21, pp. 598–604, May 2018.
[16] O. Kwon, H. G. Kim, M. J. Ham, W. Kim, G.-H. Kim, J.-H. Cho, N. I. Kim, and K. Kim, "A deep neural network for classification of melt-pool images in metal additive manufacturing," *J. Intell. Manuf.*, pp. 1–12, Oct. 2018, doi: 10.1007/s10845-018-1451-6.
[17] S. Ioffe and C. Szegedy, "Batch normalization: Accelerating deep network training by reducing internal covariate shift," in *Proc. 32nd Int. Conf. Int. Conf. Mach. Learn. (ICML)*, Lille, France, 2015, pp. 448–456.
[18] V. Nair and G. E. Hinton, "Rectified linear units improve restricted Boltzmann machines," in *Proc. 27th Int. Conf. Int. Conf. Mach. Learn. (ICML)*, Haifa, Israel, 2010, pp. 807–814.
[19] K. He, X. Zhang, S. Ren, and J. Sun, "Delving deep into rectifiers: Surpassing human-level performance on imagenet classification," in *Proc. IEEE Int. Conf. Comput. Vis. (ICCV)*, Santiago, Chile, Dec. 2015, pp. 1026–1034.
[20] I. Goodfellow, Y. Bengio, and A. Courville, *Deep Learning*. Cambridge, MA, USA: MIT Press, 2017.
[21] M. D. Zeiler, "ADADELTA: An adaptive learning rate method," Dec. 1012, *arXiv:1212.5701*. [Online]. Available: https://arxiv.org/abs/1212.5701

OHYUNG KWON received the B.S. degree in electrical engineering from the Korea Advanced Institute of Science and Technology, Daejeon, South Korea, in 2006, and the Ph.D. degree from Seoul National University, Seoul, South Korea, in 2012.

He was a Senior Engineer with the Equipment H/W Group, Mechatronics R&D Center, Samsung Electronics, Hwaseong, South Korea, until 2016. He is currently a Senior Researcher with the Additive Manufacturing Process R&D Group, Gangwon Regional Division, Korea Institute of Industrial Technology, Gangneung, South Korea. His research interest includes to apply machine learning for industry fields.

HYUNG GIUN KIM received the B.S., M.S., and Ph.D. degrees in advanced materials science and engineering from Kangwon National University, Chuncheon, South Korea, in 2007, 2010, and 2013, respectively.

He is currently a Principal Researcher with the Additive Manufacturing Process R&D Group, Gangwon Regional Division, Korea Institute of Industrial Technology, Gangneung, South Korea. His research interest includes metal additive manufacturing technologies for industrial fields, particularly with a laser.

WONRAE KIM received the B.S. degree in textile fashion engineering from the Kumoh National Institute of Technology, Gumi, South Korea, in 2005, and the M.S. degree in material engineering from Gangneung-Wonju National University, Gangneung, Korea, in 2010, where he is currently pursuing the Ph.D. degree in advanced materials engineering.

He is currently a Researcher with the Additive Manufacturing Process R&D Group, Gangwon Regional Division, Korea Institute of Industrial Technology, Gangneung. His research interest includes metal additive manufacturing technologies for industrial fields, particularly with a laser.

GUN-HEE KIM received the B.S. and Ph.D. degrees in mechanical engineering from Inha University, Incheon, South Korea, in 2003 and 2010, respectively.

He was a Researcher with the Molds & Dies R&D Group, Research Institute of Advanced Manufacturing Technology, Korea Institute of Industrial Technology, Incheon, South Korea, until 2013. He is currently a Principal Researcher with the Additive Manufacturing Process R&D Group, Gangwon Regional Division, Korea Institute of Industrial Technology, Gangneung, South Korea. His research interests include to design for additive manufacturing fields and micro finishing process.

KANGIL KIM (Member, IEEE) received the B.S. degree in computer science from the Korea Advanced Institute of Science and Technology, Daejeon, South Korea, in 2006, and the Ph.D. degree from Seoul National University, Seoul, South Korea, in 2012.

He was a Senior Researcher with the Natural Language Processing Group, Electronics and Telecommunications Research Institute, Seoul, until 2016, and an Assistant Professor with the Computer Science and Engineering Department, Konkuk University, until 2019. He is currently an Assistant Professor with the Electronics Engineering and Computer Science Department and Artificial Intelligence Graduate School, Gwangju Institute of Science and Technology, Gwangju, South Korea. His research interests include artificial intelligence, evolutionary computation, machine learning, and natural language processing.